HHS Public Access

Author manuscript

Magn Reson Imaging. Author manuscript; available in PMC 2024 January 01.

Published in final edited form as:

Magn Reson Imaging. 2023 January ; 95: 80–89. doi:10.1016/j.mri.2022.11.001.

Optimized Rectification of Fiber Orientation Density Function with Background Threshold

Hunter G. Moss[1,2], **Andreana Benitez**[1,3], **Jens H. Jensen**[1,2,4,*]

[1]Center for Biomedical Imaging, Medical University of South Carolina, Charleston, South Carolina

[2]Department of Neuroscience, Medical University of South Carolina, Charleston, South Carolina

[3]Department of Neurology, Medical University of South Carolina, Charleston, South Carolina

[4]Department of Radiology and Radiological Science, Medical University of South Carolina, Charleston, South Carolina

Abstract

Purpose: To describe an optimized fiber orientation density function (fODF) rectification procedure that removes negative values and absorbs all features below a specified threshold into a constant background.

Theory and Methods: The fODF for a white matter imaging voxel describes the angular density of axons. Because of signal noise and Gibbs ringing, fODFs estimated with diffusion MRI may take on unphysical negative values in some directions and contain spurious peaks. In order to suppress such artifacts, an fODF rectification procedure is proposed that both eliminates all negative values and incorporates all features below a specified threshold, η, into a constant background while at the same time minimizing the mean square deviation from the original, unrectified fODF. Calculating this fODF is straightforward, and the directions and shapes of peaks not absorbed into the background are preserved. The rectification method is illustrated for an analytic fODF model and for experimental diffusion MRI data obtained in healthy human brain, with the original fODFs being obtained from fiber ball imaging.

Results: Examples of optimal rectified fODFs are given for three choices of the background threshold referred to as minimal rectification ($\eta = 0$), average-level rectification ($\eta \approx 0.08$), and fractional-anisotropy-axonal-based rectification ($\eta \approx 0.1$). As η is increased, artifacts and other small features are more strongly suppressed, but the major fODF peaks are largely unaffected for the range of η values illustrated by these three alternatives.

*Corresponding author at: Department of Neuroscience, Medical University of South Carolina, Basic Science Building, MSC 510, 173 Ashley Avenue, Suite 403, Charleston, SC 29425, USA, jense@musc.edu, *Telephone*: (843)876-2467.

Author Statement

Hunter Moss: Investigation, Methodology, Software, Visualization, Writing - review & editing. **Andreana Benitez:** Funding acquisition, Writing - review & editing. **Jens Jensen**: Conceptualization, Formal analysis, Funding acquisition, Methodology, Roles/ Writing - original draft.

Declaration of Competing Interest

None.

Conclusion: Artifactual features of fODFs estimated with diffusion MRI can be effectively suppressed by applying the proposed optimized rectification procedure. Since it minimizes fODF distortion in the mean square sense, it may be useful in the study of how fODF fine structure is affected by aging and disease.

Keywords

fiber orientation density function; rectification; artifacts; axon; white matter; fiber ball imaging

1. Introduction

The fiber orientation density function (fODF) provides detailed information about the microgeometry of axons within individual white matter imaging voxels [1,2]. It can be estimated with diffusion MRI (dMRI) by using any of a variety of methods [1–9] and plays an important role in fiber tractography [10] and microstructural modeling [2,8,9,11–14]. The fODF is quantified as a function $F(\mathbf{u})$ over a spherical surface, where $\mathbf{u}$ is a unit direction vector, and it can be interpreted as the probability of a randomly selected water molecule from the intra-axonal compartment being contained inside an axon oriented parallel to $\mathbf{u}$ [2,9]. Since negative probabilities are meaningless, physically realistic fODFs must be nonnegative. However, several dMRI methods generate fODFs that can take on negative values in some directions [1–3,5,6,8,9]. This is particularly true when the fODF is represented, as is commonly done, with a spherical harmonic expansion, in which case Gibbs ringing due to truncation of the expansion and signal noise may both cause negative fODF values to occur. For this reason, it is often desirable to rectify an fODF, as the final step in its calculation, to guarantee nonnegative values for all directions.

A general method for constructing a rectified fODF that is as close as possible to an original unrectified fODF, in the mean square sense, has been described in prior work [15]. The method is straightforward to implement, simply requiring that a single parameter be determined numerically from the root of an equation constructed from the original fODF. An added benefit of this optimized rectification scheme is that fODF artifacts, such as spurious peaks due to ringing and noise, are attenuated. Nevertheless, significant artifacts may remain even after rectification that can be mistaken for true biological features and hamper comparison of fODFs for voxels from different brain regions or different subjects.

In this paper, we describe an extension of this prior rectification procedure that allows fODF artifacts to be further suppressed. The key idea is to impose an additional constraint that requires the rectified fODF for all directions in which the original fODF is less than a specified threshold, η, to be absorbed into a constant background. In this way, peaks and other fODF features smaller than η are eliminated. Here an exact solution of this extended optimization problem is given for minimizing the mean square distance between the rectified and original fODFs so that the fODF is both nonnegative and satisfies the added threshold condition. The qualitative features of this solution are similar to those for the prior rectification problem, which is recovered by setting η to zero. The solution is simple to calculate and preserves the position and shapes of all features not absorbed into the background. This rectification method constitutes a form of fODF preprocessing similar

in spirit to the type of image preprocessing routinely applied to dMRI data, with the fODF itself playing the role of an MRI image.

The main motivation for this work is to support investigation of the fine structure of fODFs rather than to aid fiber tractography, for which it is mainly the peak directions that are employed. While fiber tractography has heretofore been the predominant application of fODFs [10], improvements in scanner hardware and dMRI data processing together with recent theoretical insights are making it feasible to obtain more accurate and detailed representations for fODFs [2], thereby opening up new avenues of exploration of white matter microstructure. For such applications, simple expedients, such as setting all fODF values below a given threshold to zero, would distort fODFs more than the optimized rectification procedure proposed here.

We illustrate optimized rectification with a background threshold for an analytic fODF model based on a Watson distribution and for human dMRI data acquired at 3T using a b-value of 8000 s/mm^2. For the human data, the original fODFs are obtained with fiber ball imaging (FBI), in which the fODF is found from an inverse generalized Funk transform of the dMRI signal [2,8,16]. The effects of different choices of the background threshold are demonstrated for the number of fODF peaks and for an axon-specific diffusion anisotropy.

2. Theory

2.1. Definition of optimized rectification with background threshold

Consider an original fODF, $F(\mathbf{u})$, that has negative values in some directions and/or small peaks that one wishes to suppress. Let us assume both the antipodal symmetry

$$F(-\mathbf{u}) = F(\mathbf{u}) \tag{1}$$

and, without loss of generality, the normalization

$$\int d\Omega_{\mathbf{u}} F(\mathbf{u}) = 1, \tag{2}$$

where the integral is taken over the whole spherical surface with $|\mathbf{u}| = 1$. (This choice of normalization is adopted only for the sake of simplicity with the extension of our method to other normalizations being straightforward.) We define the optimal rectified fODF, $\hat{F}(\mathbf{u})$, as the one that minimizes the cost functional

$$C \equiv \int d\Omega_{\mathbf{u}} [\hat{F}(\mathbf{u}) - F(\mathbf{u})]^2 \tag{3}$$

subject to the constraints

$$\hat{F}(-\mathbf{u}) = \hat{F}(\mathbf{u}), \tag{4}$$

$$\int d\Omega_{\mathbf{u}} \hat{F}(\mathbf{u}) = 1, \tag{5}$$

$$\widehat{F}(\mathbf{u}) \geq 0, \tag{6}$$

and

$$\mathbf{v} \cdot \nabla \widehat{F}(\mathbf{u}) = 0, \quad \text{if } F(\mathbf{u}) < \eta, \quad \text{for any } \mathbf{v} \text{ satisfying } \mathbf{v} \cdot \mathbf{u} = 0\,. \tag{7}$$

Thus the rectified fODF will be as close as possible to the original fODF in the mean square sense, consistent with the four constraints. If the final constraint of Eq. (7) were neglected, then this would be precisely the rectification problem discussed in our prior work [15] and sufficient to define an optimal fODF that is nonnegative. Here we have added this extra constraint that sets a threshold η for the original fODF below which the rectified fODF is to be incorporated into a constant background. The vector **v** is included to specify that it is only the gradient of $\widehat{F}(\mathbf{u})$ in directions perpendicular to **u** that is relevant. In spherical coordinates, the constraint of Eq. (7) is equivalent to requiring the spherical angle derivatives of the rectified fODF to vanish for all directions **u** in which the original fODF lies below η. In this way, any peaks in the original fODF with heights below η will be suppressed and absorbed into the background. The purpose of this paper is to show how to solve for the rectified fODF defined by Eqs. (3)–(7) and demonstrate the application of this solution both for removing negative values and suppressing small fODF peaks, as may result from ringing and signal noise.

2.2. General solution

The solution to the above optimization problem involves one of three different cases, depending on the threshold η and the details of the fODF. Specifically, the applicable case depends on the values of

$$\mu \equiv \int d\Omega_{\mathbf{u}} F(\mathbf{u}) H[F(\mathbf{u}) - \eta], \tag{8}$$

where $H(x)$ is the Heaviside step function, and of a parameter ϵ that is found from the root of

$$\int d\Omega_{\mathbf{n}} [\,|F(\mathbf{n}) - \epsilon| - F(\mathbf{n}) - \epsilon] = 0. \tag{9}$$

One may verify that $\mu \geq 0$ and that $0 \leq \epsilon < F_{max}$, with F_{max} being the maximum value of $F(\mathbf{u})$ over all directions **u**. As discussed in our prior work, Eq. (9) always has exactly one root, which is easily calculated with the bisection method [15].

Case 1: If $\epsilon \geq \eta$, then the optimal rectified fODF is given by

$$\widehat{F}(\mathbf{u}) = \frac{1}{2}[\,|F(\mathbf{u}) - \epsilon| + F(\mathbf{u}) - \epsilon] = [F(\mathbf{u}) - \epsilon] H[F(\mathbf{u}) - \epsilon]\,. \tag{10}$$

This is precisely the rectified fODF obtained when the constraint of Eq. (7) is neglected [15], but if $\epsilon \geq \eta$, it automatically satisfies this equation nonetheless and thus represents the desired solution.

Case 2: If $\epsilon < \eta$ and $\mu \geq 1$, then the solution takes the form

$$\widehat{F}(\mathbf{u}) = \left[F(\mathbf{u}) - \frac{\mu - 1}{\upsilon}\right] H[F(\mathbf{u}) - \eta], \tag{11}$$

where

$$\upsilon \equiv \int d\Omega_{\mathbf{u}} H[F(\mathbf{u}) - \eta]\,. \tag{12}$$

Note that $0 \leq \upsilon \leq 4\pi$ and $\eta\upsilon \leq \mu$. By using the fact that the left side of Eq. (9) is a monotonic decreasing function of ϵ [15], one can also establish that $\mu - 1 \leq \eta\upsilon$, which guarantees that Eq. (6) is satisfied. Verifying that the constraints of Eqs. (4), (5), and (7) are also obeyed is straightforward. In the Appendix, we demonstrate that this solution minimizes the cost functional C and is therefore the optimal rectified fODF for this case.

Case 3: If $\epsilon < \eta$ and $\mu < 1$, then the solution is

$$\widehat{F}(\mathbf{u}) = F(\mathbf{u}) H[F(\mathbf{u}) - \eta] + \frac{1 - \mu}{4\pi - \upsilon} H[\eta - F(\mathbf{u})]\,. \tag{13}$$

One may readily prove that the fODF of Eq. (13) obeys the four conditions of Eqs. (4)–(7). The Appendix shows that it also minimizes C.

For all three cases, the optimal rectified fODF is a constant for $F(\mathbf{u}) < \eta$ as required by Eq. (7). If $F(\mathbf{u}) > \epsilon$, the fODF is uniformly reduced by an amount ϵ in Case 1. If $F(\mathbf{u}) > \eta$, the fODF is uniformly reduced by an amount $(\mu - 1)/\upsilon$ in Case 2 and left unchanged in Case 3. Therefore, the positions and shapes of fODF features not incorporated into the background are preserved by the rectification procedure. For both Cases 1 and 2, the background level is set to 0, while for Case 3 it is positive. When the original fODF has negative values in some directions, there will be choices of η corresponding to each of the three cases. Otherwise, only Case 3 is applicable.

As indicated by Eq. (2), we have so far only considered, for sake of simplicity, fODFs that are normalized to unity. For some applications, other normalizations are preferred [8,9,11]. In such circumstances, the Case 1 solution continues to be valid while the Case 2 and 3 solutions hold if μ is replaced by $\mu + 1 - \rho$, where ρ is the alternative normalization.

2.3. Watson distribution model

To illustrate the above rectification scheme, we apply it to a simple model fODF based on a Watson distribution [17]. For the exact fODF, we take

$$F_{ex}(\mathbf{u}) = \left[4\pi {}_1F_1\left(\frac{1}{2}; \frac{3}{2}; \kappa\right)\right]^{-1} e^{\kappa(\mathbf{u}\cdot\mathbf{n})^2}, \tag{14}$$

where $\mathbf{n}$ is a unit direction vector, ${}_1F_1(a; b; x)$ is the confluent hypergeometric function of the first kind, and κ is the concentration parameter. The Watson distribution gives physically plausible peak shapes and has been previously used to model fODFs in the context of dMRI

[18–20]. For $\kappa > 0$, it has a single peak oriented in the direction **n**. (Note that because of antipodal symmetry, there are actually two peaks at ±**n** related by reflection, but we follow the convention of counting such pairs just once.) The fODF defined by Eq. (14) is normalized according to Eq. (2), positive in all directions, and axially symmetric with respect to the direction vector **n**.

A spherical harmonic expansion for Eq. (14) can be written as

$$F_{ex}(\mathbf{u}) = \sum_{l=0}^{\infty} \sum_{m=-2l}^{2l} c_{2l}^{m} Y_{2l}^{m}(\theta, \varphi), \tag{15}$$

where (θ, φ) are the spherical angles in a coordinate system in which the polar axis is parallel to **n**, $Y_l^m(\theta, \varphi)$ are the spherical harmonic functions of degree l and order m, and c_{2l}^m are the expansion coefficients. Only even degrees enter in the sum because of antipodal symmetry. The expansion coefficients are given explicitly by

$$c_{2l}^{m} = \delta_{0m}\sqrt{4l+1}P_{2l}(0)(-\kappa)^{l}\frac{\Gamma(l+1)}{4\Gamma\left(2l+\frac{3}{2}\right)} \cdot \frac{{}_1F_1\left(l+\frac{1}{2}; 2l+\frac{3}{2}; \kappa\right)}{{}_1F_1\left(\frac{1}{2}; \frac{3}{2}; \kappa\right)} \tag{16}$$

with $P_l(x)$ being the Legendre polynomial of degree l, $\Gamma(x)$ being the gamma function, and δ_{ij} being the Kronecker delta.

When estimating fODFs from real data, one is only able to determine a finite number of the expansion coefficients (unless one makes a priori assumptions about the fODF). Therefore, spherical harmonic expansion representations of fODFs are typically truncated at a finite degree, often chosen to be 6, 8, or 10 [2]. An original estimated fODF corresponding to our Watson distribution model would then be approximated as

$$F(\mathbf{u}) = \sum_{l=0}^{L} \sum_{m=-2l}^{2l} c_{2l}^{m} Y_{2l}^{m}(\theta, \varphi), \tag{17}$$

where $2L$ is the maximum degree contained in the expansion. This expression continues to satisfy the normalization condition of Eq. (2), but because of Gibbs ringing it can have more than one peak and is not necessarily nonnegative. Hence rectification may be useful to both suppress spurious peaks and eliminate negative values.

Figure 1 shows the parameter μ as a function of η for $\kappa = 10$ and $2L = 6$. At $\eta = 0$, $\mu \geq 1$, which indicates that the original fODF has negative values. This is also reflected in a positive value for ϵ found to be about 0.0238 from Eq. (9). When $\eta \leq \epsilon$, the optimal rectified fODF is given by Case 1. When $\eta > \epsilon$ and $\mu \geq 1$, Case 2 applies. As η is further increased, μ decreases monotonically and eventually becomes less than 1 for $\eta > 0.096$, implying that the optimal fODF is provided by Case 3. A similar transition from Case 1 to 2 to 3, as η is increased, occurs whenever the original fODF has negative values. If the original fODF is positive in all directions, $\mu \leq 1$ for all η and $\epsilon = 0$. Then only Case 3 is relevant, although Cases 1, 2, and 3 become degenerate for $\eta = 0$.

The exact Watson distribution fODF of Eq. (14) for $\kappa = 10$ is shown in Figure 2A along with the corresponding original fODF obtained from Eq. (17) for $2L = 6$. Because of Gibbs ringing, the original fODF has both negative values and spurious peaks. The rectified fODF for $\eta = 0$ is plotted in Figure 2B and is an example of Case 1. All negative values have been removed, but spurious peaks remain. For $\eta = 0.05$, the rectified fODF is given in Figure 2C, which is an example of Case 2. Note that the spurious peaks have now been eliminated. An example of Case 3 with $\eta = 0.2$ is shown in Figure 2D. The background level acquires a small positive value of about 0.005 for this case. Case 3 has a nonzero background level whenever $\eta > 0$, while the background level is zero for Cases 1 and 2. As reflected in the steps of the rectified fODFs near $\theta = \pm 30°$ for Figures 2C and 2D, both Cases 2 and 3 may have discontinuities. This is always true for Case 2 and typical (but not universal) for Case 3. In contrast, the rectified fODFs for Case 1 are always continuous.

2.4. Choosing the background threshold

In applying the proposed optimized rectification procedure, one must choose a value of the background threshold η. While there are no strict constraints on η, it would normally be chosen so that $\eta \geq 0$ since the solution for $\eta < 0$ is the same as for $\eta = 0$. Also, one would typically have $\eta < F_{max}$, because for $\eta \geq F_{max}$ the rectified fODF is reduced to a simple constant for all directions. Since a sensible choice for η can depend on the intended application, the quality of the available data, and the method of fODF construction, no single prescription would cover all circumstances. There is typically a trade-off between minimizing the mean square difference between the original and rectified fODFs and suppressing artifactual features.

From the many possible ways of selecting η, we highlight three that may be useful in practice. The first is to set $\eta = 0$. That removes all negative values and gives the lowest value for the cost functional of Eq. (3). This corresponds to Case 1 and is identical to the optimized rectification scheme proposed previously [15]. We refer to the choice $\eta = 0$ as “minimal rectification”. However, minimal rectification may not always produce adequate suppression of small peaks due to ringing or noise. A stronger alternative is “average-level rectification” for which $\eta = 1/(4\pi) \approx 0.0796$. Because of the normalization condition of Eq. (2), $1/(4\pi)$ is the average value for any fODF. Setting η equal to this average, results in all fODF features below the average being absorbed into the constant background. An attractive feature of this choice is that the condition $\eta \geq F_{max}$ is automatically guaranteed, and therefore the largest fODF peak will always be retained. Finally, η can be based on the experimental data. As an illustration of this, we employ the fractional anisotropy axonal (FAA), which is a measure of intra-axonal diffusion anisotropy that can be readily calculated from the fODF and is equivalent to the axonal dispersion metric known as p_2 [13,15,16]. In particular, “FAA-based rectification” uses the largest possible value for η so that the mean FAA over all voxels of interest is at least 95% of the mean FAA for $\eta = 0$. Choosing η in this way keeps the FAA from being excessively altered and has the effect of preserving the major fODF features. The η for FAA-based rectification may, depending on the data, be larger than for average-level rectification and thereby give a stronger suppression of small peaks. In determining η, data from all subjects should be pooled to obtain a single study specific value so that consistent rectification is applied across all fODFs. Using the

same background threshold globally throughout a study is important in avoiding bias when comparing fODFs between groups that may differ in their mean FAA values. In general, η for FAA-based rectification will depend on the choice of $2L$. Of course, other quantitative measures based on the fODF could be substituted for the FAA to obtain alternative criteria for setting a background threshold, as might be suitable for some purposes.

3. Material and Methods

3.1. Imaging

Human dMRI data were acquired on a 3T Prisma^{fit} MRI system (Siemens Healthineers, Erlangen Germany) for three healthy subjects under a protocol approved by the Institutional Review Board of the Medical University of South Carolina, as previously described [2]. Two different dMRI pulse sequences were utilized – a vendor-supplied monopolar single diffusion encoding (SDE) sequence and a custom triple diffusion encoding (TDE) sequence [21]. All data were obtained with a 32 channel head coil. For the SDE sequence, the main imaging parameters were: b = 0, 1000, 2000, 8000 s/mm^2; number of diffusion encoding directions = 30 (b = 1000, 2000 s/mm^2) and 256 (b = 8000 s/mm^2); number of axial slices = 42; slice thickness = 3 mm; field of view = 222 × 222 mm^2; voxel size = 3 × 3 ×3 mm^3; TE = 99 ms; TR = 3900 ms. For b = 0, 10 volumes were collected with matched imaging parameters along with a single phase encoding reversed volume to facilitate correction of susceptibility distortion. For the TDE sequence, the imaging parameters were the same except: b-axial = 0, 4000 s/mm^2; number of diffusion encoding directions = 64; TE = 122 ms. With these settings, TDE data were obtained both with the radial gradients switched on (b-radial = 307 s/mm^2) and switched off (b-radial = 0). As for the SDE sequence, 10 TDE volumes without diffusion weighting (i.e., b-axial = b-radial = 0) were collected as well as a single phase encoding reversed volume. For anatomical reference, T1-weighted (MPRAGE) images were also acquired with: number of axial slices = 192; slice thickness = 1 mm; field of view = 256 × 256 mm^2; voxel size = 1 × 1 × 1 mm^3; TE = 2.26 ms; TR = 2300 ms; TI = 900 ms.

3.2. Data Analysis

All dMRI data were preprocessed using a pythonic version of the DESIGNER pipeline known as PyDesigner (v1.0-RC12) [22,23]. This included denoising, co-registration, and Gaussian smoothing together with corrections for Rician noise bias, Gibbs ringing, susceptibility distortion, and eddy current distortion. PyDesigner also used the SDE data with b = 0, 1000, 2000 s/mm^2 to generate maps for standard diffusional kurtosis imaging parameters [24]. Here white matter was defined as all voxels within the cerebrum having a mean kurtosis equal to or greater than 1 [25]. The TDE data were applied solely to estimate the intra-axonal diffusivity, which can be used to improve the accuracy of fODFs estimated with FBI [2], as previously described [21,26]. As dictated by FBI, fODFs were then calculated from an inverse generalized Funk transform of the SDE data for b = 8000 s/mm^2 [2,8,16]. From a computational perspective, FBI is similar to q-ball imaging [27], except that q-ball imaging employs a forward Funk transform. However, they differ fundamentally in that q-ball imaging estimates a diffusion orientation distribution function rather than an fODF [8,16].

Six white matter voxels from a single subject were selected for illustrating the effect of optimized rectification on individual fODFs. The locations of these voxels are shown in Figure 3. All white matter voxels from all three subjects were utilized for statistical analysis of the dependence on the background threshold η of the distribution of the three cases, the mean FAA, and the number of fODF peaks.

4. Results

Examples of each optimal rectification case are shown in Figure 4 for three different white matter voxels from a single subject. The fODFs were calculated with $2L = 8$ and are plotted as hemispheric equidistant azimuthal projection (HEAP) maps [2]. For this projection of a sphere onto a plane, the x-coordinate is given by $x = \theta \cos \varphi$, and the y-coordinate is given by $y = \theta \sin \varphi$, where θ and φ are the usual spherical angles. The spherical angles in the maps only cover the hemisphere defined by $0 \leq \theta < \pi/2$ and $0 \leq \varphi < 2\pi$ so that the boundary of the disks correspond to $\theta = \pi/2$. Because of antipodal symmetry, a hemisphere provides a complete description of an fODF. All fODFs are shown in a local frame of reference defined by the scatter matrix [2]. In all three voxels, the original fODFs have negative values (shown in green) as well as ringing artifacts. The negative values are eliminated in the rectified fODFs, and the ringing artifacts are suppressed. For Case 3, the ringing artifacts are completely removed, but Case 1 is closer to the original fODF in the sense of Eq. (3). Case 2 is intermediate in suppressing artifacts more strongly than Case 1 and being closer to the original fODF than Case 3. The same fODFs of Figure 4 are also given in Figure 5 as three-dimensional glyphs. This representation highlights the gross features of the fODFs, which are essentially preserved by rectification.

The fraction of voxels in which the optimal fODF corresponds to Cases 1 through 3 are plotted in Figure 6 as a function of the background threshold η for $2L = 6$, 8, and 10. The data are pooled from all the white matter voxels for all three subjects. Case 1 predominates for very small η, but when $\eta \approx 0.01$, Case 2 is most common. For $\eta > 0.05$, Case 3 is most common, and nearly all voxels are Case 3 for $\eta > 0.2$.

The mean FAA is plotted in Figure 7 as a function of η for $2L = 6$, 8, and 10. The FAA is fairly insensitive to η until $\eta \approx 0.1$, at which point it begins to decrease significantly. Similar behavior is seen for all three values of $2L$ and all three subjects. The largest value of η for which the FAA is at least 95% of its value at $\eta = 0$ is used to define FAA-based rectification and indicated by the vertical dashed lines.

Examples of minimal, average-level, and FAA-based rectification are given by Figure 8 for three voxels (different from those in Figure 3) with various numbers of major peaks. The extent to which small features are suppressed depends on the type of rectification, but the major peaks are largely unaffected. The differences in fine structure are best appreciated by comparing the fODFs for minimal and FAA-based rectification. The extent to which the major peaks are unchanged by the different rectification schemes is apparent in the three-dimensional glyphs of Figure 9.

Figure 10 shows the average number of fODF peaks per voxel as a function of η for $2L$ = 6, 8, and 10. Here both major and minor peaks are counted resulting in a large number of peaks for the lower η values. As η is increased, many of the minor peaks are absorbed into the background, and the number of peaks drops rapidly. Interestingly, a sharp drop in the number of peaks occurs near the average level of $\eta = 1/(4\pi)$, which is indicated by the black dashed lines. (For $2L = 10$, this drop occurs outside the frame of the plot.) The number of peaks increases for higher values of $2L$ since including more terms in the spherical harmonic expansion allows an fODF to exhibit more complex directional variation. For average-level rectification, the mean number peaks are 2.9, 4.9, and 10.3 for $2L$ = 6, 8, and 10, respectively. For FAA-based rectification, the corresponding peak numbers of 2.4, 4.3, and 8.6 are somewhat lower, illustrating the stronger suppression of small features for this choice of background threshold.

5. Discussion

Estimated fODFs determined from dMRI data often suffer from artifacts due to signal noise and, for spherical harmonic representations, Gibbs ringing. Both of these sources of error can lead to spurious peaks and unphysical negative values in some directions, which can hinder the application of fODFs to fiber tractography, microstructural modeling, and direct inter-subject comparisons. It is therefore of interest to filter estimated fODFs to suppress such artifacts. This is analogous to preprocessing methods, such as denoising and image distortion correction, commonly applied to diffusion-weighted brain images in order to improve quality. However, here it is preprocessing of fODF “images” for individual voxels rather than of entire brain images.

The main result of this paper is a method for constructing an optimal rectified fODF that is nonnegative and absorbs all fODF features below a specified threshold into a constant background while minimizing the mean square difference between the rectified and original fODFs. In this way, the various fODF artifacts may be suppressed. The numerical implementation of this method is straightforward, only requiring the calculation of three parameters from Eqs. (8), (9), and (12). An important property of the rectified fODFs is that the positions and shapes of all retained peaks are unchanged, although any portions of a peak lying below either ϵ or η in the original fODF are absorbed into the background. While other rectification methods for fODFs can be devised that also satisfy the conditions of Eqs. (4)–(7), these will not minimize the mean square deviation from the original fODF and thus are less likely to faithfully preserve its main features. For example, the Case 2 formula for the fODF of Eq. (11) satisfies Eqs. (4)–(7) even when Case 3 applies (i.e., if $\epsilon < \eta$ and $\mu < 1$); however, it deviates further from the original fODF than the optimal solution of Eq. (13). Considering the simplicity of the formulae for the Case 1-3 solutions, there may then be little practical advantage to employing suboptimal alternatives, even when the improvement provided by optimization is modest.

The background threshold, η, is an adjustable parameter that must be chosen in advance. This allows flexibility to tailor the rectification procedure to particular datasets and applications. Three possible background thresholds have been recommended. The first is to set $\eta = 0$, which we refer to as minimal rectification and coincides with the optimized

rectification proposed in prior work [15]. The second is (with our choice of normalization) to set $\eta = 1/(4\pi)$, which we refer to as average-level rectification and which guarantees the highest peak will always be preserved. The third is FAA-based rectification where η is adjusted to the largest value that keeps the mean FAA within 95% of its value for $\eta = 0$. Nonetheless, many other criteria for choosing η are possible, and future work may establish options that are more effective for some purposes.

We have illustrated this optimized rectification procedure both for an fODF derived from a spherical harmonic expansion of a Watson distribution model, for which negative values and spurious peaks arise only from Gibbs ringing, and for fODFs obtained from experimental data using FBI, which are affected by both Gibbs ringing and signal noise. For the experimental data, we find that, although Case 1 predominates for very small η, it applies to few voxels for $\eta > 0.05$. The fraction of voxels that are Case 2 has a maximum for $\eta \approx 0.01$ and drops to low values for $\eta > 0.1$. Above $\eta \approx 0.05$, the optimal rectified fODF is given by Case 3 in the majority of voxels. For our data, the η for FAA-based rectification is about 0.1, which provides a somewhat stronger suppression of ringing artifacts and other small fODF features than does average-level rectification. When either FAA-based or average-level rectification is applied, the mean number of fODF peaks is greatly reduced from the number found with minimal rectification, and these choices for the background threshold appear to be just adequate to suppress most of the smaller fODF peaks. Qualitatively similar results are expected for fODFs generated with alternative methods [1,3,5,6,9], but the number of voxels for each case at a given threshold setting would typically vary.

Although fODFs have been used in the context of dMRI for many years, most prior work has emphasized applications to fiber tractography, for which the directions of the main peaks are of primary interest [10]. Since the main peak positions are unaffected by the optimized rectification method proposed here, it may then have limited relevance for such applications. However, as dMRI methods and scanner hardware have improved, obtaining more detailed microstructural information from fODFs is becoming increasingly practical. The extent that this information can improve our understanding of disease, development, and aging in white matter is still underexplored [2]. As an example, there is evidence of thinner axons being lost more rapidly with aging in some white matter regions than thicker axons [28–30], but it is unknown how that alters fODFs. Since any such effects are likely subtle, a high fidelity fODF approach including optimized rectification could be useful. Thus, optimized rectification with background threshold is intended as a tool to support this exploration by helping to suppress or attenuate unphysical fODF features, which can arise as a consequence of signal noise and Gibbs ringing, while at the same time minimizing the distortion of meaningful fine structure.

6. Conclusion

A mathematically rigorous solution has been given to the problem of optimally rectifying an fODF so that the mean square deviation from the original fODF is minimized while also guaranteeing that it is nonnegative and absorbs all fODF features that lie below a specified threshold into a constant background. The solution is simple to implement numerically and suppresses spurious peaks due to signal noise and ringing artifacts. This optimized

rectification method may be useful for the investigation of changes in fODF fine structure due to aging and disease.

Acknowledgements

This work was supported by the National Institutes of Health (R01AG054159 and RF1AG057602) and by the Litwin Foundation.

Appendix

The proof that the Case 1 solution of Eq. (10) minimizes the cost functional C of Eq. (3) is presented in our prior work [15]. The corresponding arguments for Cases 2 and 3 follow similar logic and are given below.

We begin by supposing that there is an alternative fODF, $\widehat{F}'(\mathbf{u})$, that also satisfies the constraints of Eqs. (4)–(7). The difference

$$g(\mathbf{u}) \equiv \widehat{F}'(\mathbf{u}) - \widehat{F}(\mathbf{u}) \tag{A.1}$$

must then obey

$$g(-\mathbf{u}) = g(\mathbf{u}), \tag{A.2}$$

$$\int d\Omega_{\mathbf{u}} g(\mathbf{u}) = 0, \tag{A.3}$$

$$g(\mathbf{u}) \geq -\widehat{F}(\mathbf{u}), \tag{A.4}$$

and

$$\mathbf{v} \cdot \nabla g(\mathbf{u}) = 0, \quad \text{if } F(\mathbf{u}) < \eta, \quad \text{for any} \mathbf{v} \text{ satisfying } \mathbf{v} \cdot \mathbf{u} = 0\,. \tag{A.5}$$

The cost functional for $\widehat{F}'(\mathbf{u})$ is

$$C' = \int d\Omega_{\mathbf{u}} \left[\widehat{F}'(\mathbf{u}) - F(\mathbf{u})\right]^2 = \int d\Omega_{\mathbf{u}} [\widehat{F}(\mathbf{u}) - F(\mathbf{u}) + g(\mathbf{u})]^2\,. \tag{A.6}$$

This can be rewritten as

$$C' = C_0 + 2\int d\Omega_{\mathbf{u}} g(\mathbf{u})[\widehat{F}(\mathbf{u}) - F(\mathbf{u})] + \int d\Omega_{\mathbf{u}} [g(\mathbf{u})]^2, \tag{A.7}$$

with C_0 being the cost functional for $g(\mathbf{u}) = 0$.

Now let us specialize to Case 2 and apply Eq. (11) to obtain

$$C' = C_0 + 2\int d\Omega_{\mathbf{u}} g(\mathbf{u}) \left\{ \left[F(\mathbf{u}) - \frac{\mu - 1}{\upsilon} \right] H[F(\mathbf{u}) - \eta] - F(\mathbf{u}) \right\} + \int d\Omega_{\mathbf{u}} [g(\mathbf{u})]^2 \tag{A.8}$$

.

Because of Eq. (A.3), this implies

$$C' = C_0 + 2\int d\Omega_{\mathbf{u}} g(\mathbf{u})\left\{\left[F(\mathbf{u}) - \frac{\mu - 1}{\upsilon}\right]H[F(\mathbf{u}) - \eta] - F(\mathbf{u}) + \frac{\mu - 1}{\upsilon}\right\} + \int d\Omega_{\mathbf{u}}[g(\mathbf{u})]^2, \tag{A.9}$$

which is equivalent to

$$C' = C_0 - 2\int d\Omega_{\mathbf{u}} g(\mathbf{u})\left[F(\mathbf{u}) - \frac{\mu - 1}{\upsilon}\right]H[\eta - F(\mathbf{u})] + \int d\Omega_{\mathbf{u}}[g(\mathbf{u})]^2. \tag{A.10}$$

From Eq. (A.5), one sees that $g(\mathbf{u}) = k$, where k is a constant, for $F(\mathbf{u}) < \eta$. Hence, Eq. (A.10) leads to

$$C' = C_0 - 2k\int d\Omega_{\mathbf{u}}\left[F(\mathbf{u}) - \frac{\mu - 1}{\upsilon}\right]H[\eta - F(\mathbf{u})] + \int d\Omega_{\mathbf{u}}[g(\mathbf{u})]^2. \tag{A.11}$$

By using Eqs. (8) and (12), one may then verify that

$$C' = C_0 + 8\pi k \cdot \frac{\mu - 1}{\upsilon} + \int d\Omega_{\mathbf{u}}[g(\mathbf{u})]^2. \tag{A.12}$$

Since for Case 2, $\hat{F}(\mathbf{u}) = 0$ when $F(\mathbf{u}) < \eta$, Eq. (A.4) requires that $k \geq 0$. Also for Case 2, $\mu \geq 1$ by assumption. Hence the middle term on the right side of Eq. (A.12) is nonnegative. From this it follows that

$$C' \geq C_0 + \int d\Omega_{\mathbf{u}}[g(\mathbf{u})]^2. \tag{A.13}$$

Therefore, in Case 2, Eq. (11) is the optimal rectified fODF that minimizes the cost functional.

For Case 3, we apply Eq. (13) to Eq. (A.7) to find

$$C' = C_0 + 2\int d\Omega_{\mathbf{u}} g(\mathbf{u})\left[\frac{1 - \mu}{4\pi - \upsilon} - F(\mathbf{u})\right]H[\eta - F(\mathbf{u})] + \int d\Omega_{\mathbf{u}}[g(\mathbf{u})]^2. \tag{A.14}$$

Just as for Case 2, $g(\mathbf{u}) = k$ for $F(\mathbf{u}) < \eta$, although the constant k is now not necessarily positive. We then see that

$$C' = C_0 + 2k\int d\Omega_{\mathbf{u}}\left[\frac{1 - \mu}{4\pi - \upsilon} - F(\mathbf{u})\right]H[\eta - F(\mathbf{u})] + \int d\Omega_{\mathbf{u}}[g(\mathbf{u})]^2. \tag{A.15}$$

The integral in the middle term on the right side of Eq. (A.15) vanishes as a consequence of Eqs. (8) and (12). Thus Eq. (A.13) holds once again, showing that Eq. (13) is indeed the optimal rectified fODF for Case 3.

Abbreviations:

dMRI	diffusion Magnetic Resonance Imaging

FBI	fiber ball imaging
fODF	fiber orientation density function
FAA	fractional anisotropy axonal
HEAP	hemispheric equidistant azimuthal projection
SDE	single diffusion encoding
TDE	triple diffusion encoding

References

1. Tournier JD, Calamante F, Gadian DG, Connelly A. Direct estimation of the fiber orientation density function from diffusion-weighted MRI data using spherical deconvolution. NeuroImage 2004;23:1176–1185. [PubMed: 15528117]
2. Moss H, Jensen JH. High fidelity fiber orientation density functions from fiber ball imaging. NMR Biomed 2022;35: e4613. [PubMed: 34510596]
3. Tournier JD, Calamante F, Connelly A. Robust determination of the fibre orientation distribution in diffusion MRI: non-negativity constrained super-resolved spherical deconvolution. NeuroImage 2007;35:1459–1472. [PubMed: 17379540]
4. Dell'Acqua F, Rizzo G, Scifo P, Clarke RA, Scotti G, Fazio F. A model-based deconvolution approach to solve fiber crossing in diffusion-weighted MR imaging. IEEE Trans Biomed Eng 2007;54:462–472. [PubMed: 17355058]
5. Kaden E, Anwander A, Knösche TR. Variational inference of the fiber orientation density using diffusion MR imaging. NeuroImage 2008;42:1366–1380. [PubMed: 18603006]
6. Yeh FC, Wedeen VJ, Tseng WY. Estimation of fiber orientation and spin density distribution by diffusion deconvolution. NeuroImage 2011;55:1054–1062. [PubMed: 21232611]
7. Cheng J, Deriche R, Jiang T, Shen D, Yap PT. Non-negative spherical deconvolution (NNSD) for estimation of fiber orientation distribution function in single-/multi-shell diffusion MRI. NeuroImage 2014;101:750–764. [PubMed: 25108182]
8. Jensen JH, Glenn GR, Helpem JA. Fiber ball imaging. NeuroImage. 2016;124:824–833. [PubMed: 26432187]
9. Dell'Acqua F, Tournier JD. Modelling white matter with spherical deconvolution: How and why?. NMR Biomed 2019;32:e3945. [PubMed: 30113753]
10. Jeurissen B, Descoteaux M, Mori S, Leemans A. Diffusion MRI fiber tractography of the brain. NMR Biomed 2019;32:e3785. [PubMed: 28945294]
11. Riffert TW, Schreiber J, Anwander A, Knösche TR. Beyond fractional anisotropy: extraction of bundle-specific structural metrics from crossing fiber models. NeuroImage 2014;100:176–191. [PubMed: 24936681]
12. Novikov DS, Veraart J, Jelescu IO, Fieremans E. Rotationally-invariant mapping of scalar and orientational metrics of neuronal microstructure with diffusion MRI. NeuroImage 2018;174:518–538. [PubMed: 29544816]
13. McKinnon ET, Helpern JA, Jensen JH. Modeling white matter microstructure with fiber ball imaging. NeuroImage 2018;176:11–21. [PubMed: 29660512]
14. Novikov DS, Fieremans E, Jespersen SN, Kiselev VG. Quantifying brain microstructure with diffusion MRI: Theory and parameter estimation. NMR Biomed 2019;32:e3998. [PubMed: 30321478]
15. Moss HG, Jensen JH. Optimized rectification of fiber orientation density function. Magn Reson Med 2021;85:444–455. [PubMed: 32710476]
16. Moss HG, McKinnon ET, Glenn GR, Helpern JA, Jensen JH. Optimization of data acquisition and analysis for fiber ball imaging. NeuroImage 2019;200:690–703. [PubMed: 31284026]
17. Watson GS. Equatorial distributions on a sphere. Biometrika 1965;52:193–201.

18. Zhang H, Hubbard PL, Parker GJ, Alexander DC. Axon diameter mapping in the presence of orientation dispersion with diffusion MRI. NeuroImage 2011;56:1301–1315. [PubMed: 21316474]
19. Zhang H, Schneider T, Wheeler-Kingshott CA, Alexander DC. NODDI: practical in vivo neurite orientation dispersion and density imaging of the human brain. NeuroImage 2012;61:1000–1016. [PubMed: 22484410]
20. Coelho S, Pozo JM, Jespersen SN, Jones DK, Frangi AF. Resolving degeneracy in diffusion MRI biophysical model parameter estimation using double diffusion encoding. Magn Reson Med 2019;82:395–410. [PubMed: 30865319]
21. Ramanna S, Moss HG, McKinnon ET, Yacoub E, Helpern JA, Jensen JH. Triple diffusion encoding MRI predicts intra-axonal and extra-axonal diffusion tensors in white matter. Magn Reson Med 2020;83:2209–2220. [PubMed: 31763730]
22. Ades-Aron B, Veraart J, Kochunov P, McGuire S, Sherman P, Kellner E, Novikov DS, Fieremans E. Evaluation of the accuracy and precision of the diffusion parameter Estimation with Gibbs and NoisE removal pipeline. NeuroImage 2018;183:532–543. [PubMed: 30077743]
23. Dhiman S, Teves JB, Thorn KE, McKinnon ET, Moss HG, Adisetiyo V, Ades-Aron B, Veraart J, Chen J, Fieremans E, Benitez A. PyDesigner: A pythonic implementation of the DESIGNER pipeline for diffusion tensor and diffusional kurtosis imaging. bioRxiv 2021. doi: 10.1101/2021.10.20.465189.
24. Jensen JH, Helpern JA. MRI quantification of non-Gaussian water diffusion by kurtosis analysis. NMR Biomed 2010;23:698–710. [PubMed: 20632416]
25. Yang AW, Jensen JH, Hu CC, Tabesh A, Falangola MF, Helpern JA. Effect of cerebral spinal fluid suppression for diffusional kurtosis imaging. J Magn Reson Imaging 2013;37:365–371. [PubMed: 23034866]
26. Jensen JH, Helpern JA. Characterizing intra-axonal water diffusion with direction-averaged triple diffusion encoding MRI. NMR Biomed 2018;31:e3930. [PubMed: 29727508]
27. Tuch DS. Q-ball imaging. Magn Reson Med 2004;52:1358–1372. [PubMed: 15562495]
28. Marner L, Nyengaard JR, Tang Y, Pakkenberg B. Marked loss of myelinated nerve fibers in the human brain with age. J Comp Neurol 2003;462:144–152. [PubMed: 12794739]
29. Fan Q, Tian Q, Ohringer NA, Nummenmaa A, Witzel T, Tobyne SM, Klawiter EC, Mekkaoui C, Rosen BR, Wald LL, Salat DH. Age-related alterations in axonal microstructure in the corpus callosum measured by high-gradient diffusion MRI. Neuroimage 2019;191:325–336. [PubMed: 30790671]
30. Dhiman S, Fountain-Zaragoza S, Jensen JH, Falangola MF, McKinnon ET, Moss HG, Thorn KE, Rieter WJ, Spampinato MV, Nietert PJ, Helpern JA. Fiber ball white matter modeling reveals microstructural alterations in healthy brain aging. Aging Brain 2022;2:100037. [PubMed: 36324695]

Highlights

- Method for optimized rectification of fiber orientation density functions is given.
- All features below a specified threshold are absorbed into a constant background.
- Negative values are eliminated, and spurious peaks are suppressed.
- Mean square deviation from the original function is minimized.
- The method is easily implemented, and the directions of major peaks are unaltered.

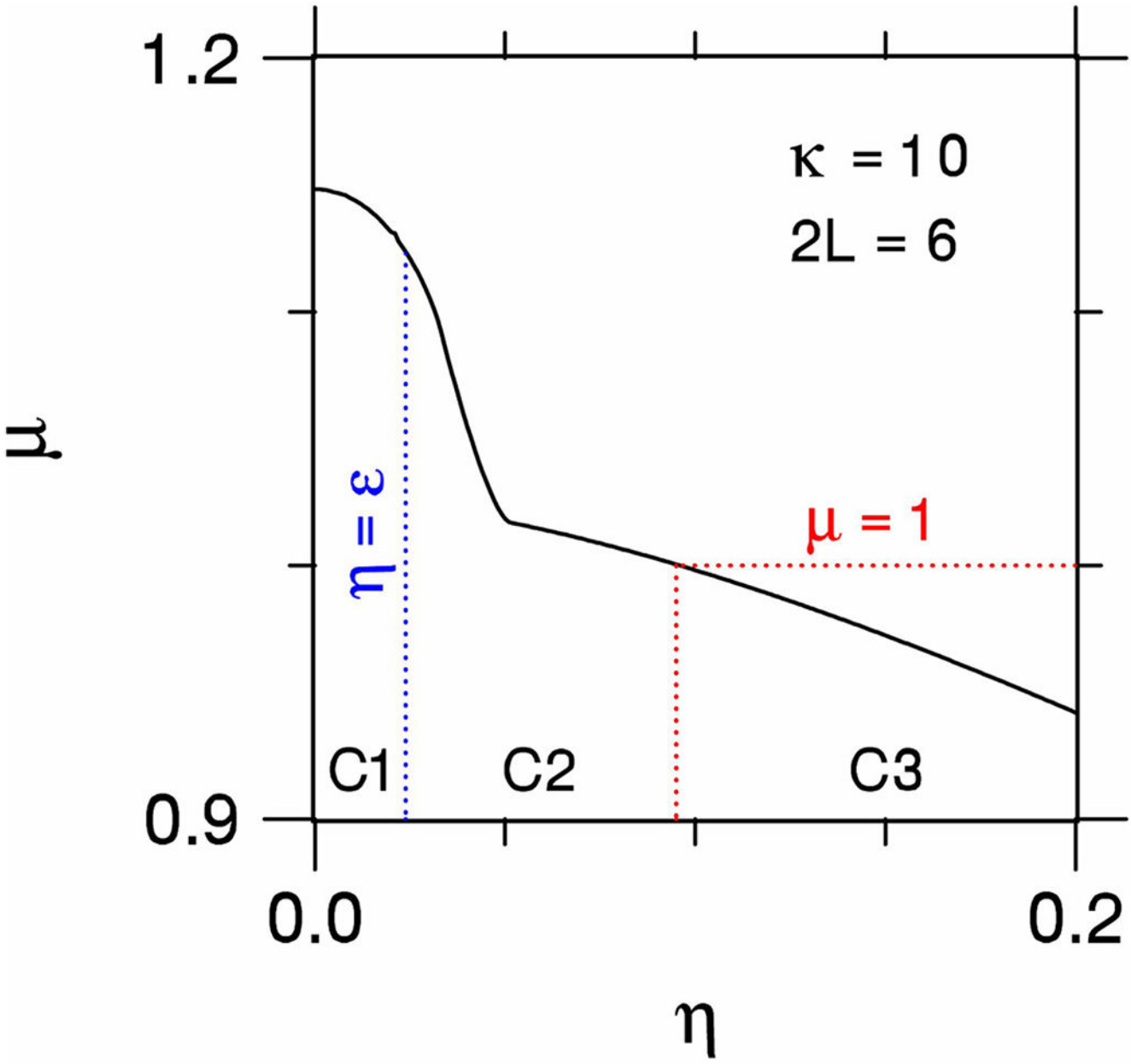

Figure 1.

The parameter μ as a function of the background threshold η for the Watson distribution fODF of Eq. (14) with $\kappa = 10$ when represented as a spherical harmonic expansion having a maximum degree $2L = 6$. For small η, $\mu > 1$ indicating that the fODF has negative values, and μ decreases monotonically to zero as η is increased. For $\eta \leq \epsilon$, the optimal rectified fODF is given by Case 1 (C1) of Eq. (10). For $\eta > \epsilon$ and $\mu \geq 1$, Case 2 (C2) of Eq. (11) provides the optimal rectified fODF. In all other circumstances, the optimal rectified fODF is the Case 3 (C3) expression of Eq. (13).

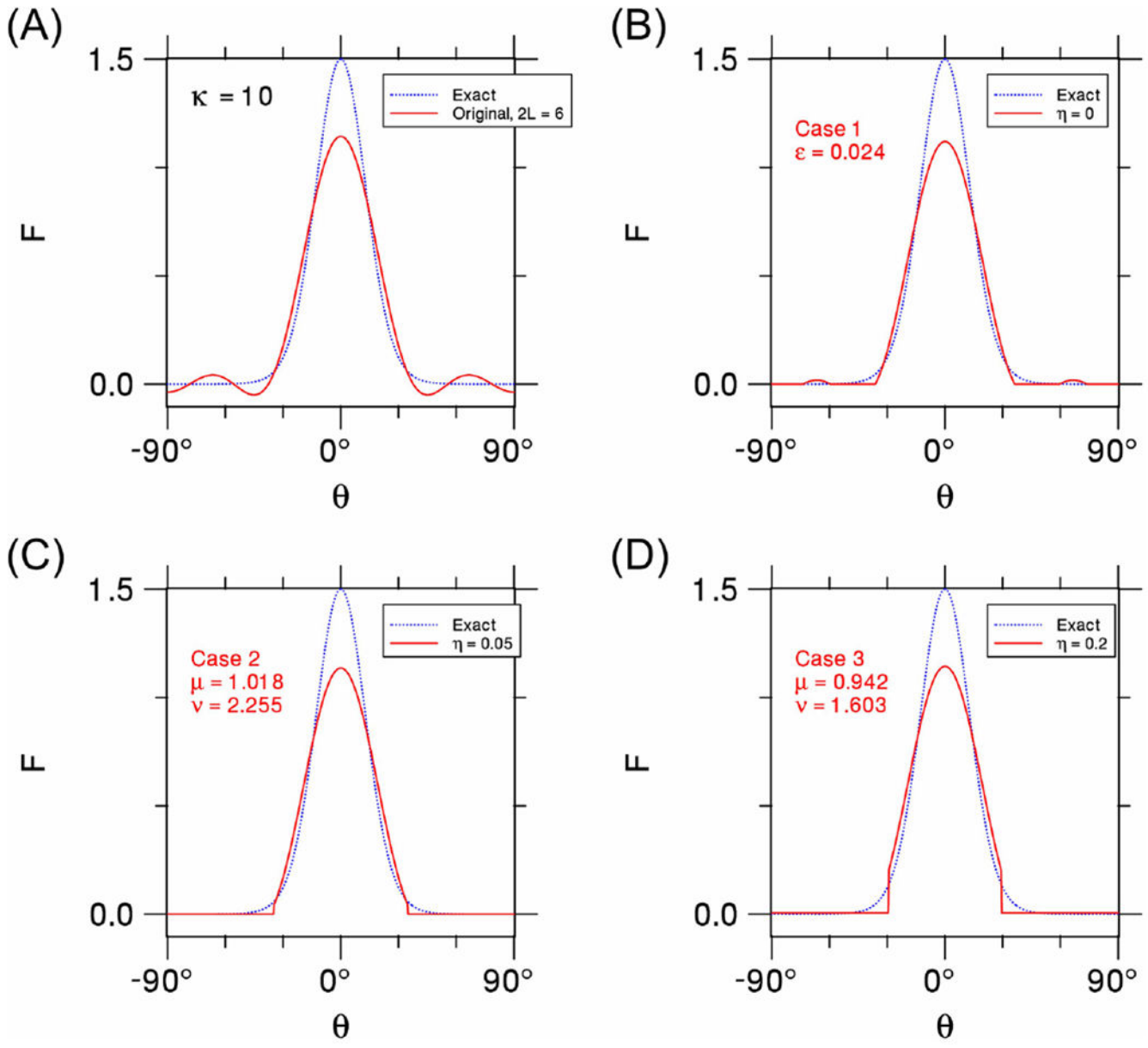

Figure 2.

(A) Original fODF (red solid line) for a Watson distribution with $\kappa = 10$ as approximated with a spherical harmonic expansion having a maximum degree $2L = 6$. The exact fODF (blue dotted line) is shown as a reference (A-D). Both the original and exact fODFs are axially symmetric and plotted as functions of the polar angle θ. Note that the original fODF has both negative values and ringing artifacts. (B) Rectified fODF (red solid line) with $\eta = 0$, corresponding to Case 1. All negative values are eliminated but ringing artifacts remain. (C) Rectified fODF (red solid line) with $\eta = 0.05$. This is an example of Case 2. Both the negative values and the ringing artifacts have been removed. The main peak is only slightly altered in comparison to the original fODF, and the background level is zero. (D) An example of Case 3 with a background threshold of $\eta = 0.2$. The background level is slightly

positive (≈ 0.005) although this is difficult to discern in the figure. All fODFs, including the three rectified cases, are normalized according to Eq. (2).

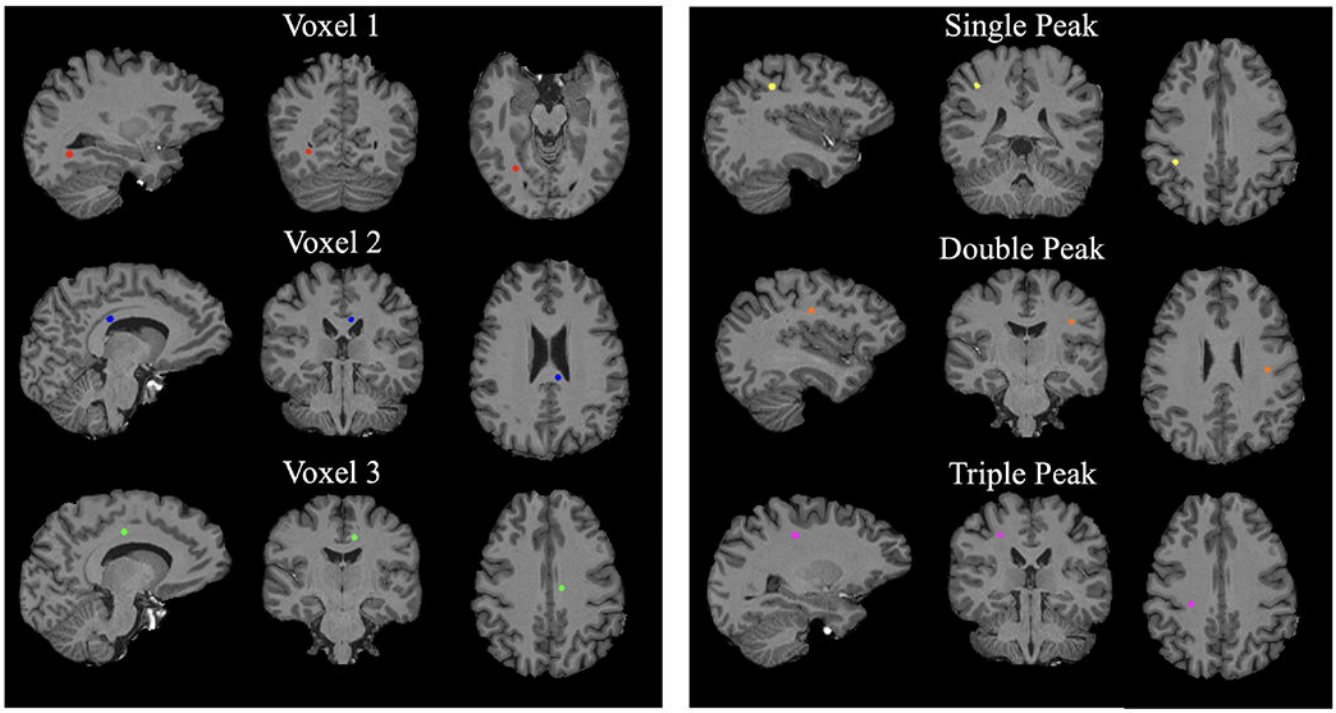

Figure 3.

Locations of six different white matter voxels selected for illustrating the effect of optimized rectification on individual fODFs. Voxels are indicated by colored circles superimposed on T1-weighted anatomical images. All voxels shown were obtained from a single subject.

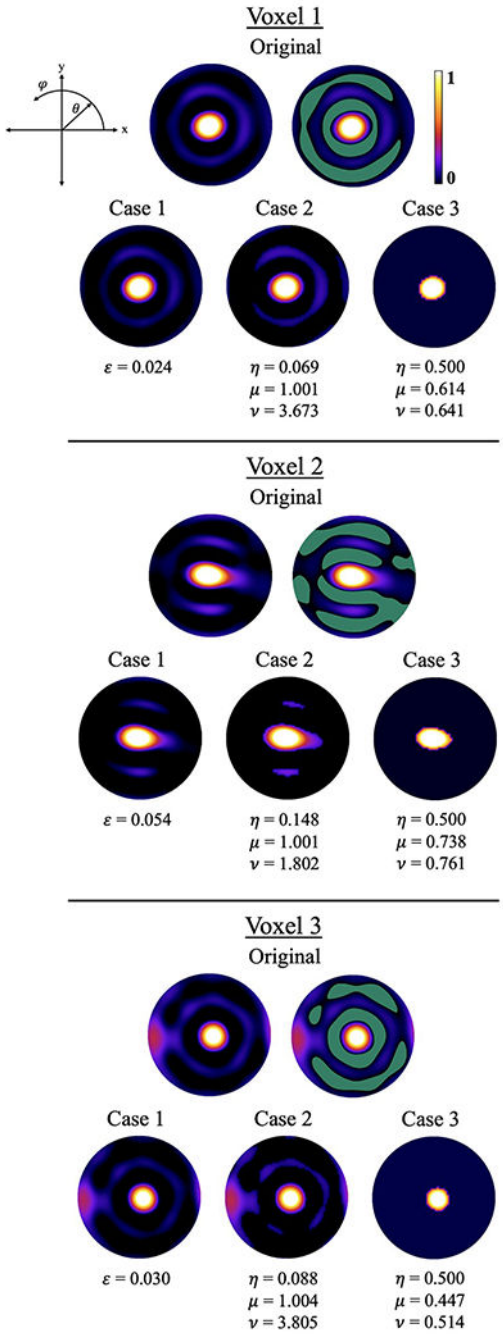

Figure 4.

Hemispheric equidistant azimuthal projection (HEAP) maps of fODFs for three different white matter voxels illustrating the three different cases of optimized rectification. The HEAP map intensities reflect the value of the fODF in a given direction and are all windowed from 0 to 1. For the original fODFs, two HEAP maps are shown, which are identical except the rightmost maps have directions with negative values highlighted in green. Ringing artifacts are apparent for all three fODFs. By construction, all negative values are eliminated in the rectified fODFs of Cases 1-3. In Case 1, negative values are removed

with minimal change from the original fODF, and the background level set to zero. In Case 2, the background threshold η is increased to further suppress artifacts while the background level remains at zero. The ringing artifacts are completely removed for Case 3, and the background level is greater than zero. All fODFs are calculated with $2L = 8$. Voxel locations are shown in the left panel of Figure 3.

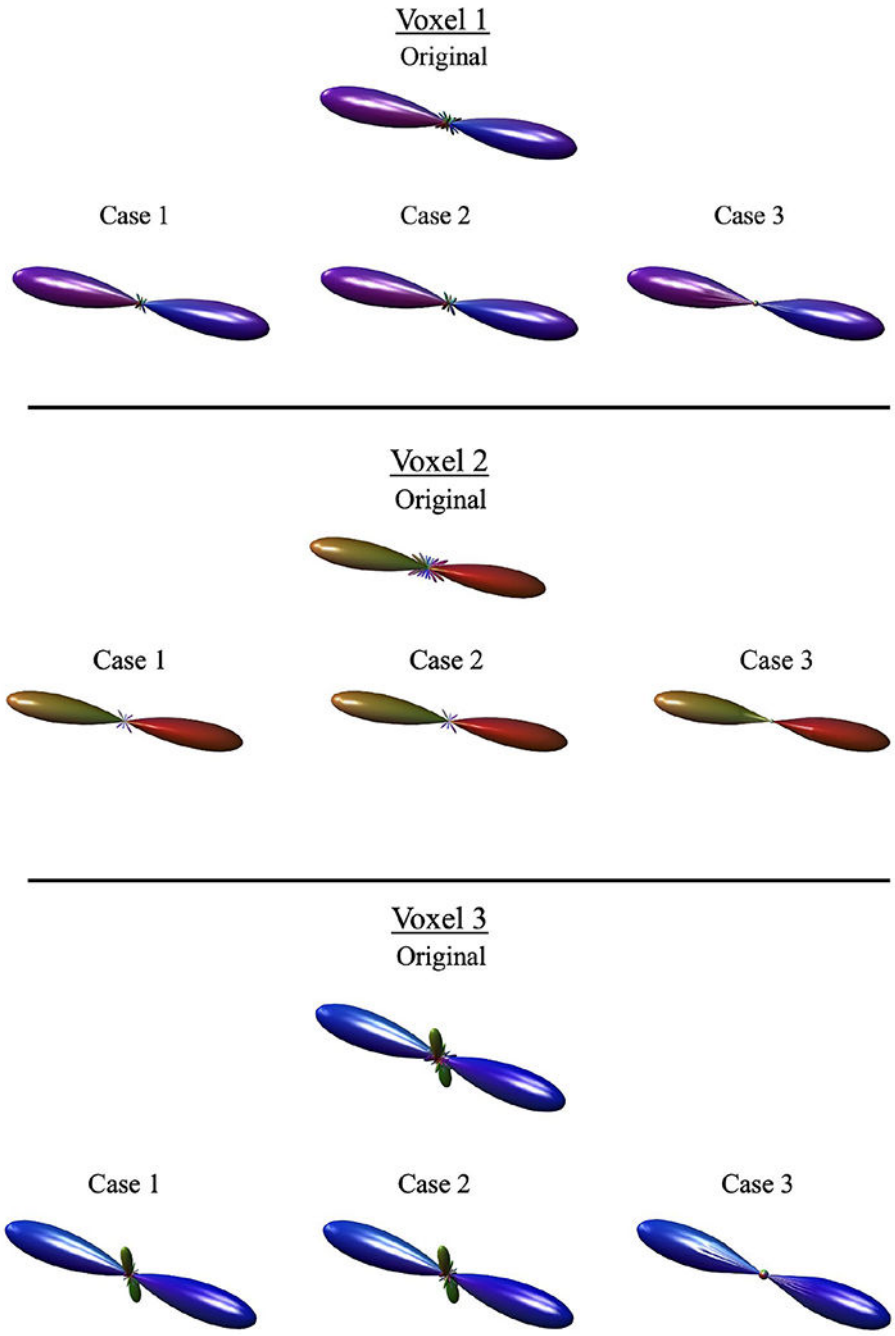

Figure 5.
Three-dimensional glyphs for the same fODFs shown in Figure 4. The glyphs emphasize the gross features of the fODFs, which are largely unchanged by optimized rectification.

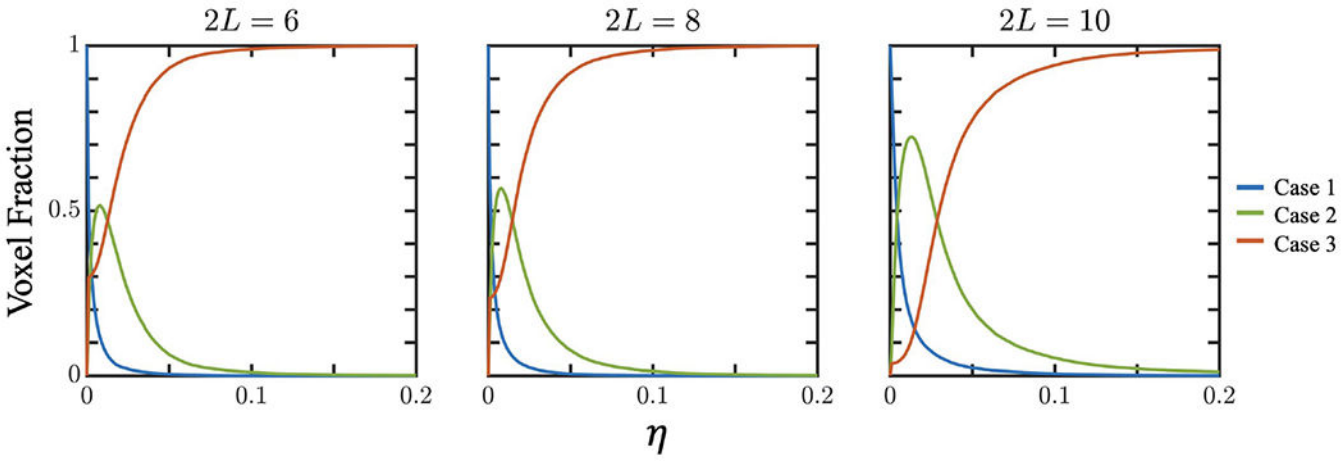

Figure 6.

Fraction of white matter voxels in which the optimal rectification corresponds to Case 1, 2, or 3 as a function of the background threshold η for whole white matter data pooled from all three subjects. For very small η, Case 1 (blue line) predominates, but very few voxels correspond to Case 1 for $\eta > 0.05$, depending somewhat on $2L$. Case 2 (green line) predominates for $\eta \approx 0.01$, but few Case 2 voxels remain for $\eta > 0.1$. If $\eta > 0.05$, Case 3 (red line) is the most common, and nearly all voxels correspond to Case 3 for $\eta > 0.2$.

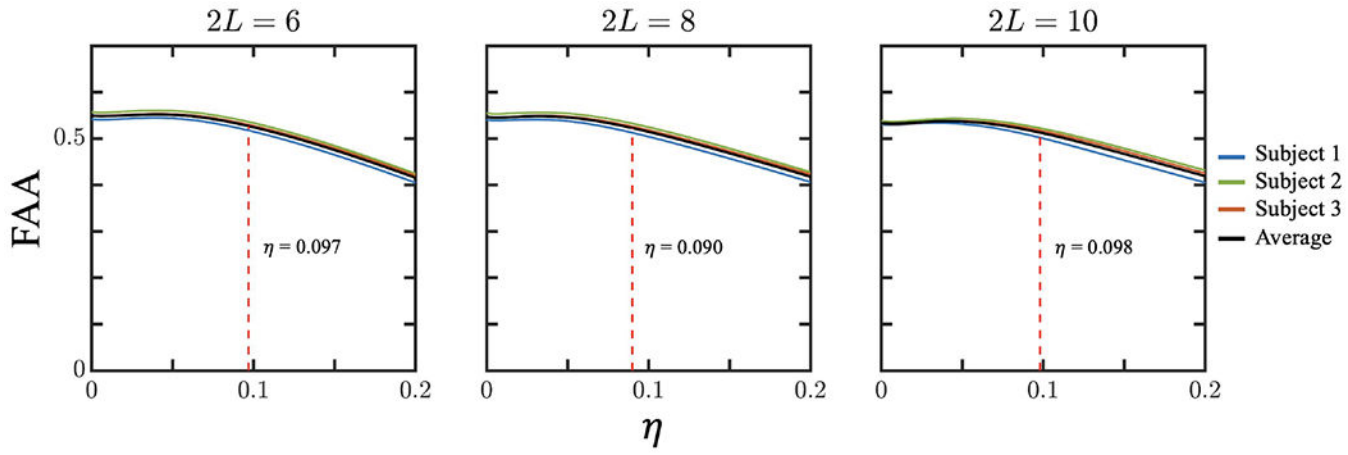

Figure 7.

Mean fractional anisotropy axonal (FAA) versus η over whole white matter for three subjects (colored lines) along with the group average (black line). The FAA is affected by the choice of η and decreases for $\eta \gtrsim 0.05$ as the impact of rectification becomes more pronounced. The η values at which the FAA is reduced to 95% of the value for $\eta = 0$ are indicated by the vertical dashed lines. This value may be used to define FAA-based rectification and is approximately 0.1 for all three values of $2L$ considered.

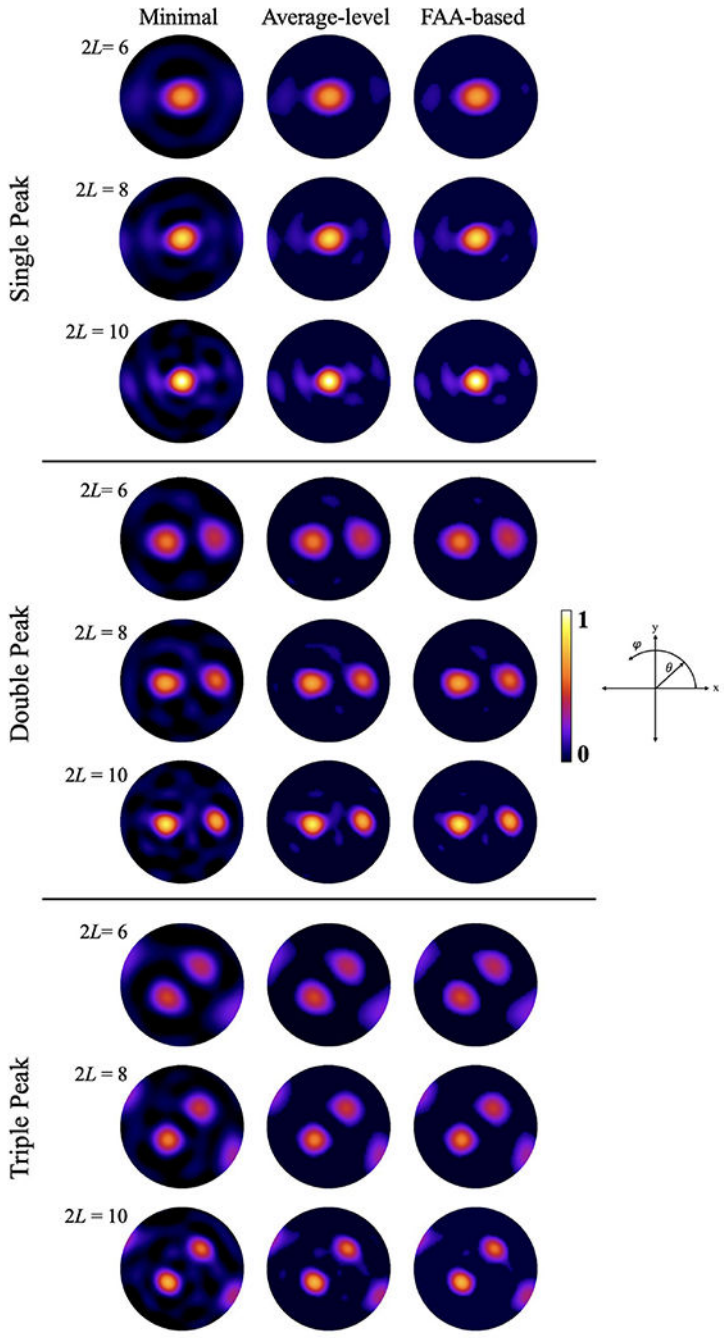

Figure 8.

HEAP maps showing examples fODFs with minimal, average-level, and FAA-based rectification for three voxels with one, two, or three major peaks. Each type of rectification typically corresponds to a different choice for η. Minimal rectification applies whenever $\eta \leq \epsilon$ while average-level rectification has $\eta = 1/(4\pi) \approx 0.080$. With FAA-based rectification, our data gives η values of 0.097 for $2L = 6$, 0.090 for $2L = 8$, and 0.098 for $2L = 10$. The main peaks are only slightly affected by the choice of rectification but the extent small features are suppressed varies considerably. This is most apparent when comparing fODFs

for the minimal and FAA-based rectification. Voxel locations are shown in the right panel of Figure 3.

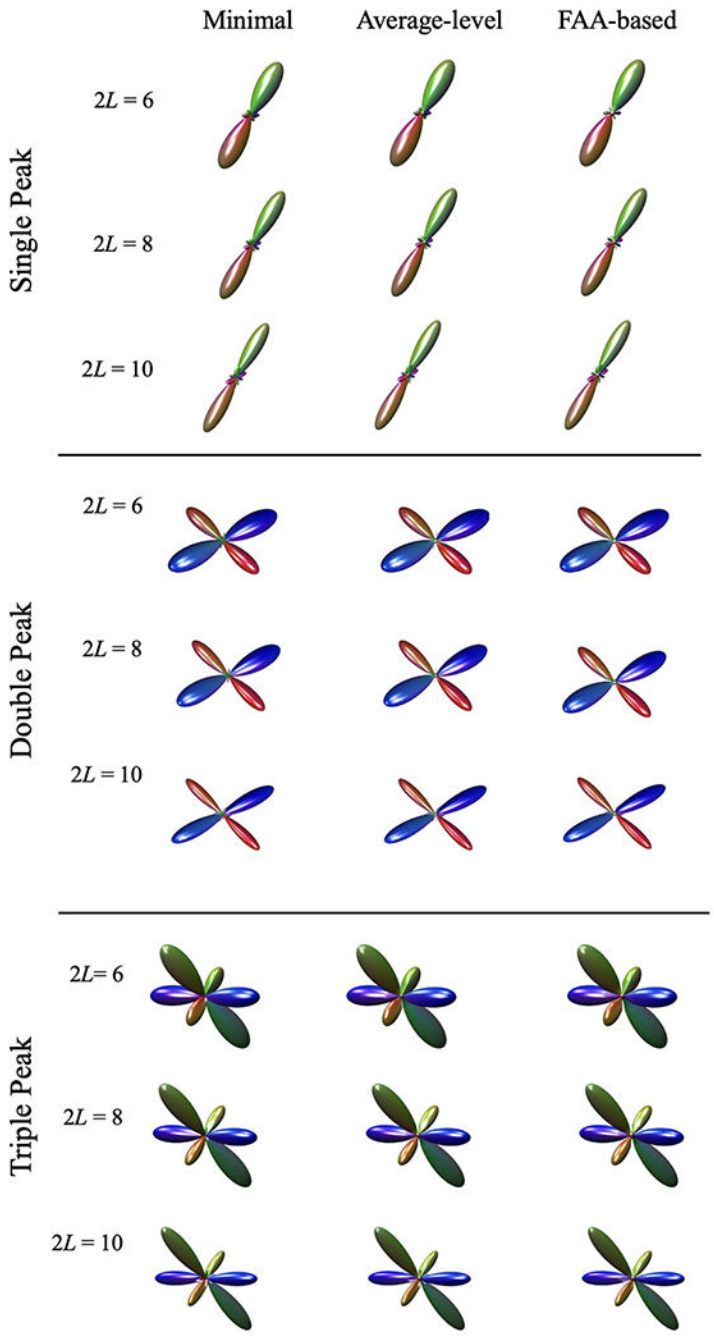

Figure 9.

Three-dimensional glyphs for the same fODFs shown in Figure 8. The major fODF peaks for the three different types of optimized rectification are nearly identical for the three different choices of the background threshold.

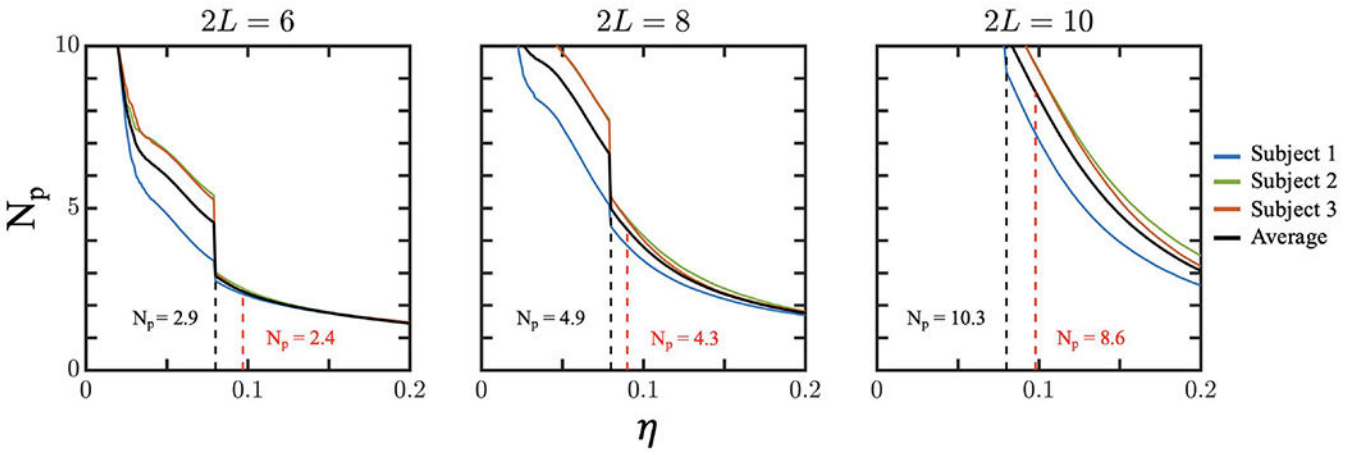

Figure 10.

The mean number of fODF peaks of any size per voxel (N_p) versus η over whole white matter for three subjects (colored lines) along with the group average (black line). Increasing η sharply decreases the number of peaks by absorbing small features into the background. The black dashed lines indicate η for average-level rectification while the red dashed lines show η for FAA-based rectification. Notice the sharp drop in the number of peaks at the background threshold for average-level rectification in the plots for $2L = 6$ and $2L = 8$. A similar drop occurs for $2L = 10$, but is outside the range of the data shown. The number of peaks increases with $2L$ since a higher number of terms in the harmonic expansion for an fODF accommodates more structural detail.